POLITECNICO DI TORINO
Repository ISTITUZIONALE

Enhanced Bandwidth Tunability in Thermally Controlled Multi-pitch Contra-directional Couplers

Original
Enhanced Bandwidth Tunability in Thermally Controlled Multi-pitch Contra-directional Couplers / Tunesi, L., Curri, V., Carena, A., Bardella, P.. - In: IEEE PHOTONICS JOURNAL. - ISSN 1943-0655. - ELETTRONICO. - 17:4(2025), pp. 1-11. [10.1109/jphot.2025.3576041]

Availability:
This version is available at: 11583/3001130 since: 2026-03-11T16:35:52Z

Publisher:
IEEE

Published
DOI:10.1109/jphot.2025.3576041

Terms of use:

This article is made available under terms and conditions as specified in the corresponding bibliographic description in the repository

Publisher copyright
IEEE postprint/Author's Accepted Manuscript

©2025 IEEE. Personal use of this material is permitted. Permission from IEEE must be obtained for all other uses, in any current or future media, including reprinting/republishing this material for advertising or promotional purposes, creating new collecting works, for resale or lists, or reuse of any copyrighted component of this work in other works.

(Article begins on next page)

28 November 2026

Enhanced bandwidth tunability in thermally controlled multi-pitch contra-directional couplers

Lorenzo Tunesi, Vittorio Curri, Andrea Carena, and Paolo Bardella

***Abstract*—Grating-Assisted Contra Directional Couplers (GACDCs) are versatile photonic devices which can implement free-spectral-range free add-drop flat-top responses, making them interesting solutions for Wavelength Division Multiplexing (WDM) systems and many other applications requiring spectral shaping. Their bandwidth can be dynamically changed through thermal means, granting an additional degree of freedom in their design and application. Design techniques involving the periodicity of the gratings (pitch chirping) can enhance the effect of this dynamic control, leading to wider bandwidth tunability in terms of both central channel wavelength and passband width, while leaving the control mechanism and power unchanged. In this work, we investigate the limits of these effects, highlighting the advantages through simulation of both the optical response and the thermal control.**

***Index Terms*—Grating Assisted Couplers, Bragg Grating, Add-Drop Filters, Bandwidth flexible**

I. Introduction

The field of Photonic Integrated Circuits (PICs) is seeing a significant increase in interest due to the high performance capabilities introduced by integration [1], [2], as well as the wide range of applications[3]. Using programmable and flexible components, PICs are expected to enable advancement in both the optical communication landscape, representing the more traditional application scenario, as well as adjacent fields, such as photonic computing, sensing, biomedical, and more[4].

In the telecom and datacom fields, which represents the main target of this work, one of the main challenges is the control of the light, which allows dynamic switching of the signals toward the target destination[5]. In today's optical communications, the standard application is represented by Wavelength-Division Multiplexing (WDM), where different frequencies are used to encode the channels, requiring therefore components able to split and route different spectral slices. Modern-day paradigms, such as software defined networking [6], require elastic and flexible elements, capable of dynamic wavelength allocation and flexible reconfiguration. The flexibility of operation in this context is represented by the ability to dynamically change both the central wavelength and the channel 3 dB bandwidth.

Many different photonic building blocks can be used to implement frequency-selective filtering elements[7], such as Micro Ring Resonators (MRRs)[8], [9], Mach-Zehnder Interferometers (MZIs)[10], Arrayed Waveguide Gratings (AWGs)[11], and many more, but due to their advantageous properties and wide design space, our work focuses on Grating-Assisted Contra Directional Couplers (GACDC).

GACDCs are extremely versatile photonic devices that can implement a wide variety of functions, ranging from reflectors, mode and polarization multiplexers/converters[12], [13], and frequency selective add-drop filters[14]. Their core operation is based on Bragg gratings[15], which are arranged in a two-waveguide coupling structure to achieve precise control of the propagation and modal evolution of the electromagnetic field[16]. In their application as WDM multiplexers / demultiplexers (MUX / DEMUX)[17], they offer some advantages over competing integrated solutions, as they can implement wide-band flat-top filters with steep roll-offs [18], which is ideal for modern Dense WDM (DWDM) applications with high channel count and minimal spacing in the frequency comb. Moreover, GACDCs can also be dynamically tuned to tailor the 3 dB bandwidth and central wavelength of the filtered channel, allowing the deployment of these devices for flexible and elastic optical switches. Different control techniques can be used to this end, with thermo-optic tuning being the most common and straightforward method: the optical properties of the material can be adjusted by varying the temperature of the waveguides throughout the device by means of micro heaters.

In this work, we present an in-depth analysis of this dynamic control available through thermo-optical means, investigating how segmented thermal control, together with modulation of the grating periodicity, can be used to increase the dynamic tunablity range: through analytical modelling of the optical propagation, as well as multiphysics heat simulations of the micro-heaters, we highlight the limiting factors and range of this control scheme.

II. GACDC design and simulation model

GACDCs are four-port integrated photonic components obtained by introducing a periodic perturbation in an otherwise uncoupled asymmetric two-waveguide device. The structure consists of two asymmetric waveguides, that is, presenting a different effective mode index, which are spatially separated to limit or eliminate traditional co-directional coupling, as shown in Fig. 1a. By introducing a periodic perturbation of the effective index along the field propagation direction, which is done through modulation of the waveguide widths, the structure can be designed to introduce frequency-selective coupling between the forward propagating mode of the input waveguide and the backward propagating mode of the second waveguide. The operating principle behind the contradirectional coupling is based on Bragg gratings[19], which act as distributed wavelength-selective mirrors along the structure,

Lorenzo Tunesi, Vittorio Curri, Andrea Carena, and Paolo Bardella are with the Department of Electronics and Telecommunications at Politecnico di Torino, Turin 10126, Italy.
Corresponding authors: lorenzo.tunesi@polito.it, paolo.bardella@polito.it

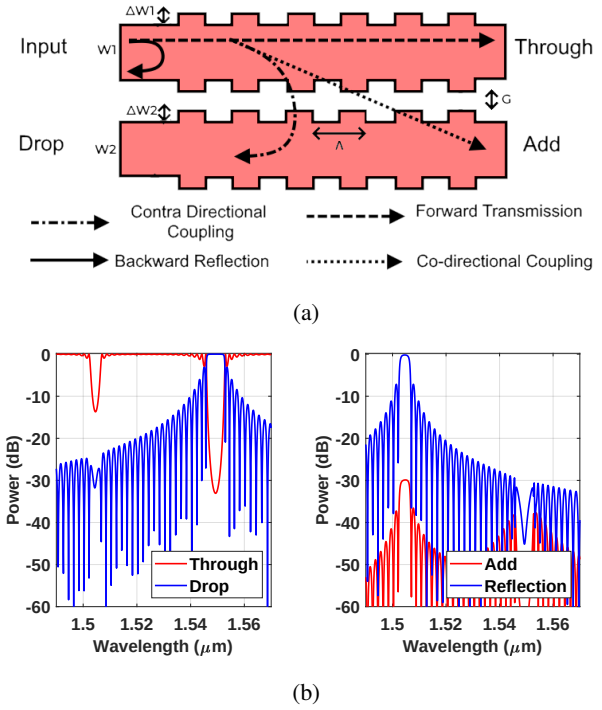

Fig. 1: **(a)** Generic GACDC geometry highlighting the main coupling effects for the input signal. **(b)** Typical frequency response at the four ports of a GACDC (the reflection peak represent the signal reflected backwards from the input port).

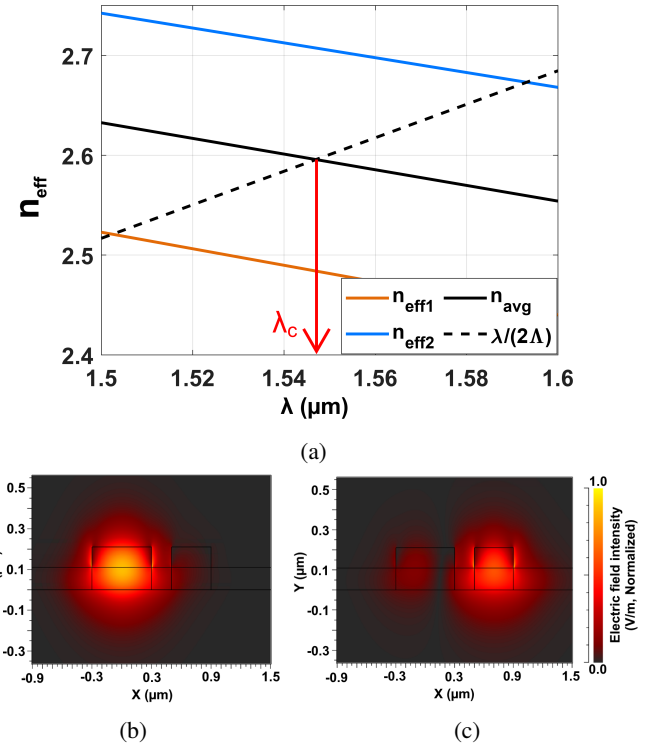

Fig. 2: **(a)** Effective index plot for the two waveguides highlighting the phase match condition. **(b)** First coupled mode of the GACDC structure. **(c)** Second coupled mode of the GACDC structure.

with their design and the asymmetric waveguide geometry allowing for a wide range of frequency responses[20].

Observing the response for a standard GACDC device, depicted in Fig. 1b, three main coupling effects can be identified. Part of the input spectrum is reflected backwards to the input port, due to the Bragg grating of the first waveguide; the channel of interest is coupled contra-directionally to the second waveguide, exiting the drop port, while the rest of the spectrum is propagated to the through port. Some parasitic co-directional coupling may arise toward the add port, although it is usually minimized due to the high distance between the intrinsic waveguide. The GACDC is a reciprocal device; as such, while the channel of interest is dropped from the input waveguide toward the Drop port, the same wavelength-dependent selectivity is present at the Add port, which means that a new signal on the same channel can be multiplexed from the Add port back onto the main waveguide toward the Through port.

The design of the intrinsic waveguide geometry and the index perturbation is what controls the magnitude of these effects, as well as the coupling frequency: the channel frequency can be understood by considering the phase-match condition of the structure, as depicted in Fig. 2a. Due to the asymmetry of the structure, the modes in the two waveguides propagate with different effective indices, with the grating enabling contra-directional coupling only under the Bragg condition or phase-match condition: this frequency is represented by the intersection between the curve obtained from the Bragg grating pitch Λ, and the average effective index of the unperturbed geometry. The magnitude of the coupling effect is instead related to the modal overlap between the super-modes supported by the two grating-enhanced waveguides, which are represented for a reference ridge geometry in Fig. 2b-c. In these devices, the two unperturbed waveguides should instead be ideally uncoupled, with only the grating region that allows modal overlap under the Bragg condition[21]: this is done to minimize unwanted directional coupling, which only introduces crosstalk and additional losses.

A. *Simulation model*

In this work the GACDC are modeled using the well-established Coupled Mode Theory (CMT) formulation [19], [22], which is implemented and run using MATLAB. The model allows for a rapid and computationally inexpensive characterization of the devices, which is convenient with respect to other numerical simulation methods available in commercial-level photonic simulation suites, such as Finite-Difference Time-Domain (FDTD) or EigenMode Expansion (EME). Due to the length of the GACDC devices (up to millimeters) and the required high simulation resolution (due to the typical submicrometer grating pitch), the computational cost to run analysis of the propagating electromagnetic field is unfeasible using the former generic numerical methods. The CMT formulation is, instead, inexpensive to run, while maintaining relatively high accuracy if the parameters are properly fitted. In the CMT model, the structure geometry is abstracted considering the effective indices, propagation constants, and coupling coefficients, which can be extracted

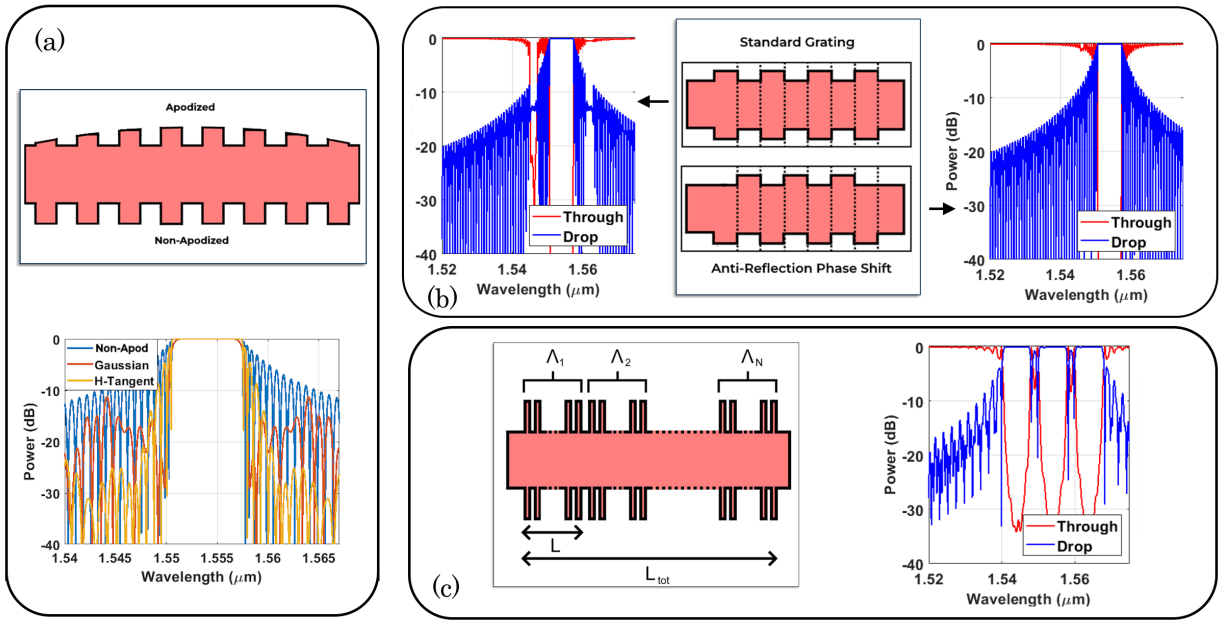

Fig. 3: **(a)** Example of apodized profile and comparison of non-apodized device response against gaussian and hyperbolic tangent apodized structure. **(b)** Effect of the antireflection phase shift, with highlight of the intrawaveguide reflection minimization in the response. **(c)** Example of a pitch-chirped device exhibiting three adjacent drop windows.

from the geometry using accurate numerical methods. In our case, this was accomplished using the RSoft Photonic design suite[23], leading to an optimized simulation model, where the static characterization of the waveguide geometry, materials, and properties is carried out through physics-based numerical methods, while the field propagation is instead carried out through the more efficient CMT analytical approach.

B. Design

The analysis presented in this work aims to characterize the limits and maximum ranges for the thermal mechanism of bandwidth tuning, while envisioning applications in a WDM system. As such, there is no univocal solution and design choice which can fit all possible applications, although the analysis and the design choices of a specific case can be generalized to offer insight into the flexibility of these devices, and more specifically the optimized strategy for the thermal control.

As stated, GACDC offer a wide design space, as both the waveguide geometry and grating structures can be engineered to change the resulting response, also allowing complex multi-channel coupling structures[24]: depending on the application many trade-offs may arise, typically related to either performance, tolerances, circuit footprint, or a combination of the previous.

However, for the implementation as single channel adaptable filters, there are some key design choices which help improve the filter performance, reducing the parasitic effects, improving selectivity, or increasing the bandwidth tunability. These strategies are summarized in Fig. 3, which highlight the three main techniques: corrugation width apodization, anti-reflection gratings, and pitch chirping.

GACDCs drop response suffers from large side-channel ripples, which can limit their deployment in dense WDM systems. These sidelobes, which represent the Fabry-Pérot modes of the waveguides introduced by the Distributed Bragg Reflector, can be mitigated by reducing the reflectivity in the trasition region between the unperturbed waveguides and the DBR section. This is typically achieved by smoothing the transition to the high-coupling region, either by decreasing the corrugation amplitude or leveraging the phase mismatch between the gratings on the two waveguides [25]. The example in Fig. 3a shows the effect on the drop frequency response as a function of the amplitude apodization, comparing the default response against the resulting channel using Gaussian or hyperbolic tangent profiles [26].

The other major undesired effect in the response of GACDCs is the intra-waveguide reflection introduced by the gratings of both waveguides. These regions should fall outside of the drop response, thanks to the asymmetric waveguide design, although they still limit the application in cascaded device, as well as introducing an unwanted back-propagating signal in the main waveguide. This effect can be mitigated by designing the corrugation with a π-shift between the two sides of the waveguide [27]. The out-of-phase design does not affect the inter-waveguide coupling, while introducing destructive interference on the intra-waveguide reflection, canceling the peak (Fig. 3b).

The last design choice to take into account addresses the device bandwidth instead of a parasitic unwanted effect. The periodicity of the grating can be slowly changed throughout the device, introducing multiple adjacent phase-match conditions[28]. This technique allows for not only an extension of the static bandwidth (i.e. without electrical control signals),

but also its tunabilityΔBW, defined as the difference between the maximum ($\Delta\lambda_{\max}$) and minimum ($\Delta\lambda_{\min}$ passband widths that can be obtained through an external electrical control. This approach, called pitch chirping, can be used both to create multichannel devices and to increase the drop bandwidth Fig. 3c [29]; its effect is discussed in more detail in the following section.

All the above design techniques have been considered for the reference device, which is used as a benchmark for the subsequent analysis: the waveguide and grating geometry have been chosen to synthesize a flat-top filter centered in the middle of the C-band ($\lambda_{\text{ch}} = 1.55\,\mu\text{m}$), designed on the Silicon Photonic platform. The silicon waveguides are simulated with thickness $h = 220\,\text{nm}$, widths $w_1 = 570\,\text{nm}$ and $w_2 = 450\,\text{nm}$, separated by a gap $G = 200\,\text{nm}$ and $L_{\text{tot}} = 450\,\mu\text{m}$ long; the grating structure has been simulated with pitch $\Lambda = 298\,\text{nm}$, corrugation widths $\Delta w_1 = 100\,\text{nm}$ and $\Delta w_2 = 60\,\text{nm}$ and a hyperbolic tangent apodization profile ($f(x) = \left[1+\tanh\left(\beta\left(1-2\,|x|^{\alpha}\right)\right)\right]$ with $\alpha = 3$, $\beta = 3$). and assuming a propagation loss of $3\,\text{dB/cm}$ for the simulated devices,which represents a conservative estimates based on experimental measurements of comparable devices.[28].

III. Bandwidth Tunability

The main mechanism to achieve 3 dB bandwidth tunability in GACDC is the modulation of the phase match condition across the longitudinal direction of the device: this can be achieved through different means, either through dynamic adjustment of the waveguide indices (thermo-optic or electro-optic effects) or the adjustment of the grating pitch Λ. This principle of operation is shown in Fig. 4: by changing either the waveguide or grating properties, the drop wavelength can be adjusted, with the pitch chirping representing the static solution to create wide-band or multichannel behavior during design, and the thermal effect representing the dynamic reconfigurable adjustment.

Considering only the effect on the drop window central frequency, it is clear how the pitch chirping behaves equivalently as an hard-coded temperature offset, while at the same time still allowing for the dynamic temperature control. In general, the bandwidth can be controlled by tuning the different sections of the device, increasing or decreasing the overlap between adjacent phase-match spectral regions as the overall device response is simply obtained as a cascade of the different regions. In this analysis the dynamic control of the index is assumed to be based on silicon thermo-optic effect, which is used to introduce the index shift through a temperature gradient across the longitudinal direction. Accounting for the temperature shift in the aforementioned CMT simulation model is quite straightforward, as silicon behavior can be easily modeled through its thermo-optical coefficient ($\frac{dn}{dT} \approx 1.86 \times 10^{-4}\,\text{K}^{-1}$) which does not vary significantly for reasonable temperature shifts [30]. However, it is necessary to simulate the thermal behavior in more depth, as the maximum temperature shift is dictated by the microheater technology used in the integrated chip, and the thermal crosstalk must also be considered to ensure proper gradient control.

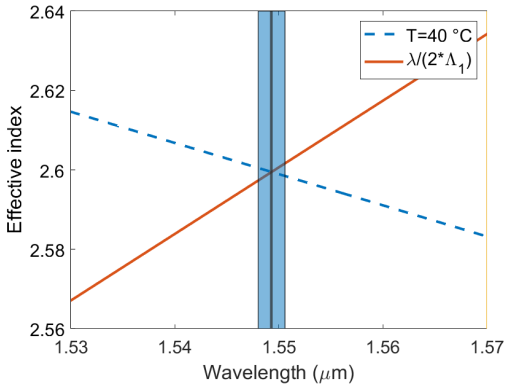

(a)

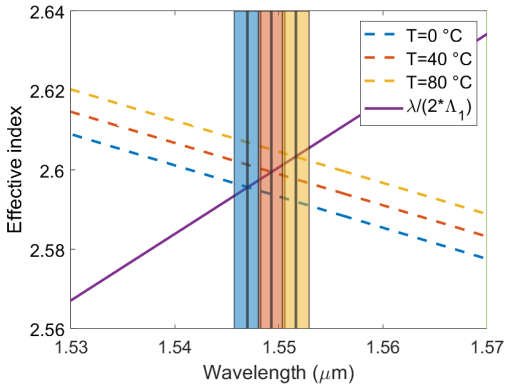

(b)

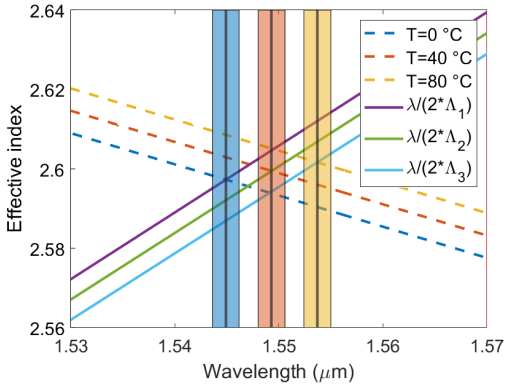

(c)

Fig. 4: Phase match condition curves highlighting the channel region. **(a)** Single phase-match condition considering reference bias temperature and single pitch. **(b)** Effect of the waveguides temperature. **(c)** Effect of the waveguides temperature and multiple grating pitches.

A. Thermal modeling

Thermal simulations require a clearly defined layer geometry to account for heat dissipation as well as heater placement and material: in our analysis we have considered the IC layers available in the Silicon Photonic platform from Applied Nanotool Fig. 5a (ANT)[31]. The structure has been simulated through COMSOL Multiphysics, considering a single microheater spine that runs the length of the device, with

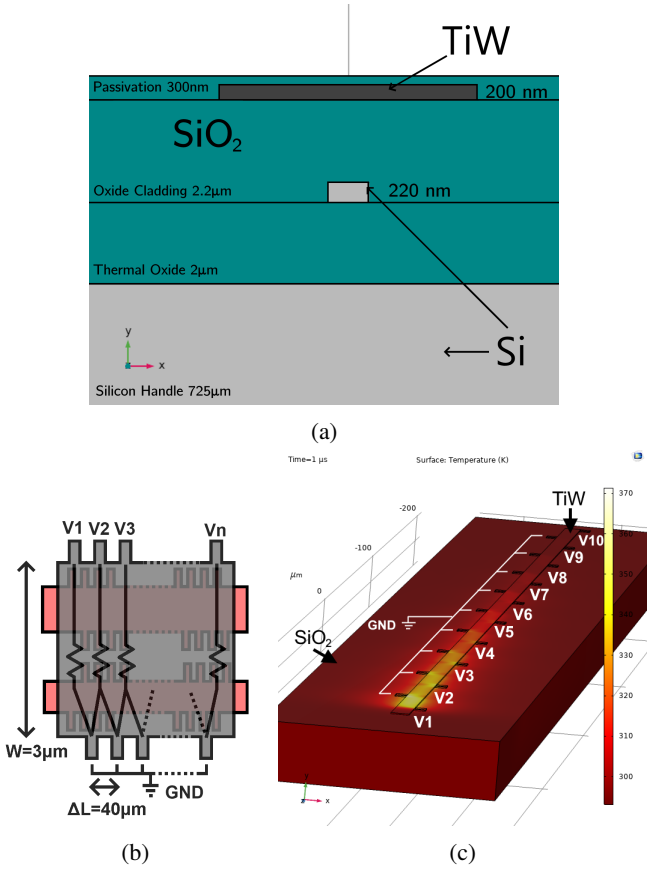

Fig. 5: **(a)** ANT layer geometry used in the simulation. **(b)** Generic Structure of the heater element. **(c)** Thermal gradient simulation of the segmented heater on a simplified oxide layer stack.

multiple contact points on both sides, allowing precise control of the voltage gradient across the structure Fig. 5b. The rib is modeled with width $W = 3\,\mu\text{m}$, contact spacing $\Delta L = 40\,\mu\text{m}$, and ten contact points: the structure can be seen as a series of parallel resistors running orthogonally to the light propagation direction, allowing control over the temperature gradient. The advantage of such configuration is that it can achieve multi-section control without requiring separated heating structures, leveraging instead a single grounded side and the current flowing through the least resistance path. This type of heater has been shown to work in providing flexible control in single pitch structures [32], and in this analysis, it has been simulated assuming ten contact points along the length of the device.

The layers and materials have been defined in COMSOL, using the multiphysics Electromagnetic Heating module, which uses the Electrical Current model together with the Heat Transfer in Solids to simulate Joule heating and the heat diffusion of the geometry. In this simulation, the control mechanism is modeled as a voltage applied directly to the contact pads on the side of the main heater spine, without considering the routing layer which would connect the heater contacts to the external pads (Fig. 5c): the thermal effect of the routing connections is typically negligible, as a low-resistivity material is used with respect to the high resistivity of the Titanium Tungsten (TiW) heater.

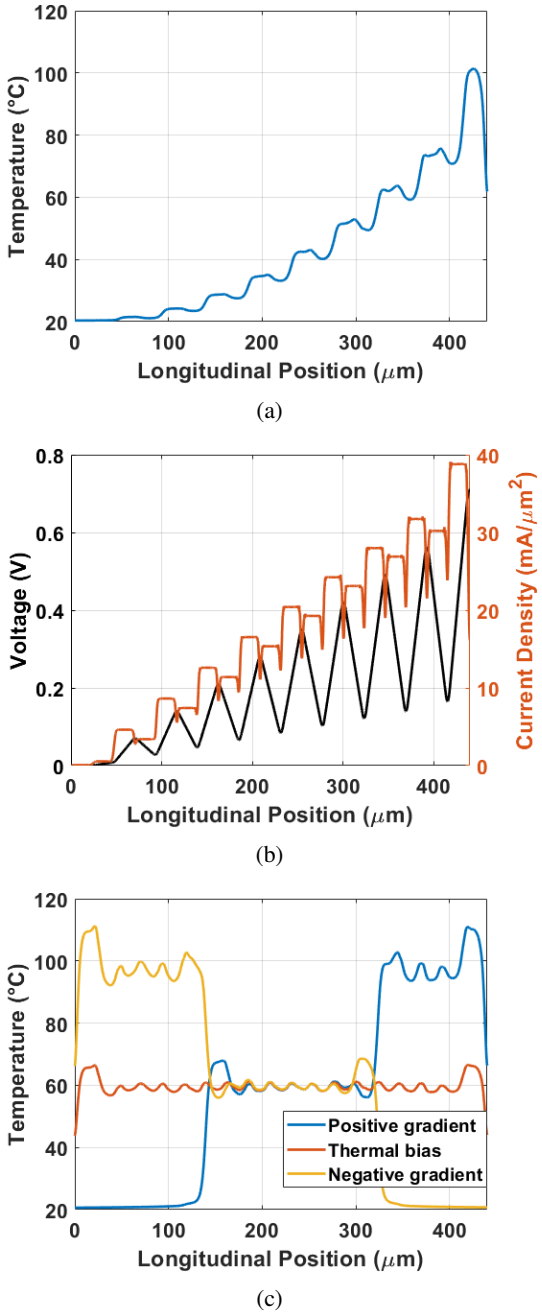

Fig. 6: **(a)** Maximum temperature gradient achievable with the proposed heater structure. **(b)** Voltage across the center of the TiW heater and resulting current density. **(c)** Example of piecewise thermal control along the heater spine.

In the depicted heater simulation, the layer stack and simulation box are simplified to improve readability, excluding the passivation layer to show the metallic heater geometry, highlighting the nine ground contacts (left side) as well as the ten voltage control points (right side).

In the actual simulation the heater has been instead placed in the center of the simulation box, considering a die with footprint $1\,\text{mm} \times 1\,\text{mm} \times 0.73\,\text{mm}$ and uniform layer composition (following ANT layer structure). In order to obtain any meaningful result, the thermal boundary conditions must be

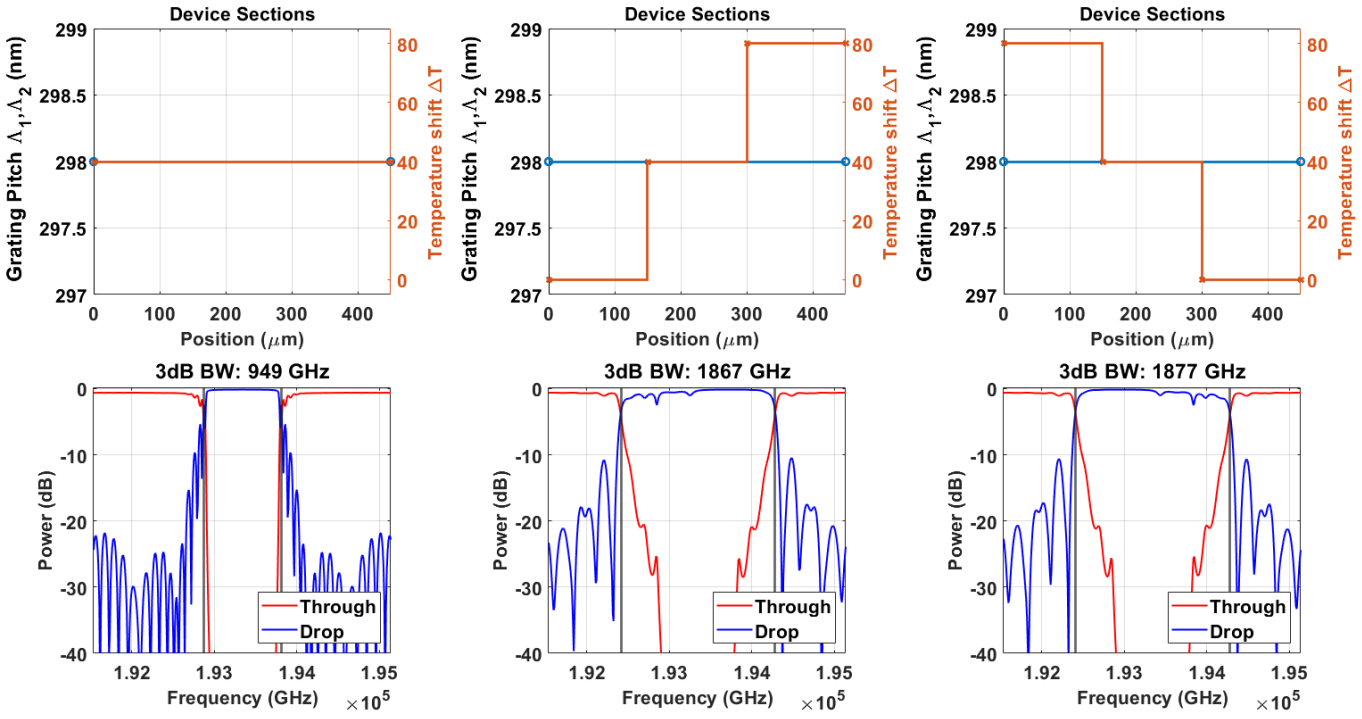

(a) (b) (c)

Fig. 7: Drop bandwidth for the single pitch device: a) at default state b) under positive thermal chirp c) under negative thermal chirp.

set up properly, allowing correct heat dissipation of the die. In our analysis we have considered convective heat flux with a coefficient $h = 10\,\mathrm{W/m^2/K}$ on the top and lateral faces of the chip, which correspond to natural external convection through air. The bottom face is instead modeled as an ideal heat sink, providing a Dirichlet boundary condition ($T_{\mathrm{ext}} = 23\,^{\circ}\mathrm{C}$), which is standard practice in the thermal analysis of integrated circuits [33]. The maximum achievable thermal shift can be evaluated by applying a voltage gradient across the contacts, considering the limitation imposed by the maximum current density through the microheater (maximum safe operating value provided by ANT as $J = 5\,\mathrm{mA/\mu m^2}$). From the simulation, we see that temperatures around $T = 100\,^{\circ}\mathrm{C}$ can be obtained (Fig. 6a) while keeping the overall current density in the heater below the threshold (Fig. 6b): considering the ambient temperature, we obtain a $\Delta T = 80\,^{\circ}\mathrm{C}$ thermal offset that can be used to calibrate and tune the device bandwidth. Moreover, Fig. 6c presents some of the piecewise step temperatures that can be obtained throughout the device, which will be used in the following section to explore the tunability range.

B. GACDC dynamic control

As stated before, the mechanism to dynamically adjust the bandwidth is based on introducing and controlling the overlap between multiple phase-match regions. Starting with the simple case of a single pitch device (Fig. 7, we can see the limiting factor imposed by the temperature gradient. For the default state, a thermal offset of $\Delta T = 40\,^{\circ}\mathrm{C}$ is considered, as it allows a consistent central wavelength even when temperature gradients are applied [34], which leads to a reference bandwidth of $\mathrm{BW} = 949\,\mathrm{GHz}$ (Fig. 7a): this is the same value as the static bandwidth at ambient temperature $\Delta T = 0\,^{\circ}\mathrm{C}$, but shifted around a different wavelength. When a thermal gradient is applied, the bandwidth can increase up to $\mathrm{BW} = 1867\,\mathrm{GHz}$ as shown in Fig. 7b-c, although due to the single pitch, both positive and negative temperature gradients produce identical results: the mirrored losses seen at the edges of the drop response are due to the propagation losses used in the simulation, which affect the phase-match region further along the propagation direction.

An improvement with respect to the first design can be seen in the pitch-chirped structure, where we assume a three-pitched region with value $\Lambda_1 = 297\,\mathrm{nm}$, $\Lambda_2 = 298\,\mathrm{nm}$, $\Lambda_3 = 299\,\mathrm{nm}$. The pitch step $\delta\lambda = 1\,\mathrm{nm}$ has been chosen based on previous ultra-large bandwidth passive GACDC designs[28], which have been realized on the same technological platform. In this work the study is limited to three pitch regions to highlight the tuning principle, while the effect of the manufacturing uncertainty will be briefly discussed in the later section.

The multiple phase-match conditions allow for a noticeable extension of the static bandwidth, with a value of $\mathrm{BW} = 1847\,\mathrm{GHz}$ (Fig. 8a). Apart from the increase in 3 dB bandwidth, the real advantage of this design can be observed when a positive or negative thermal gradient is applied (Fig. 8b-c): while a positive thermal bias increases the bandwidth, as in the single-pitch case, up to $\mathrm{BW} = 2766\,\mathrm{GHz}$, a negative gradient can be used to reduce the bandwidth with respect to the static case, down to the reference bandwidth of $\mathrm{BW} = 949\,\mathrm{GHz}$.

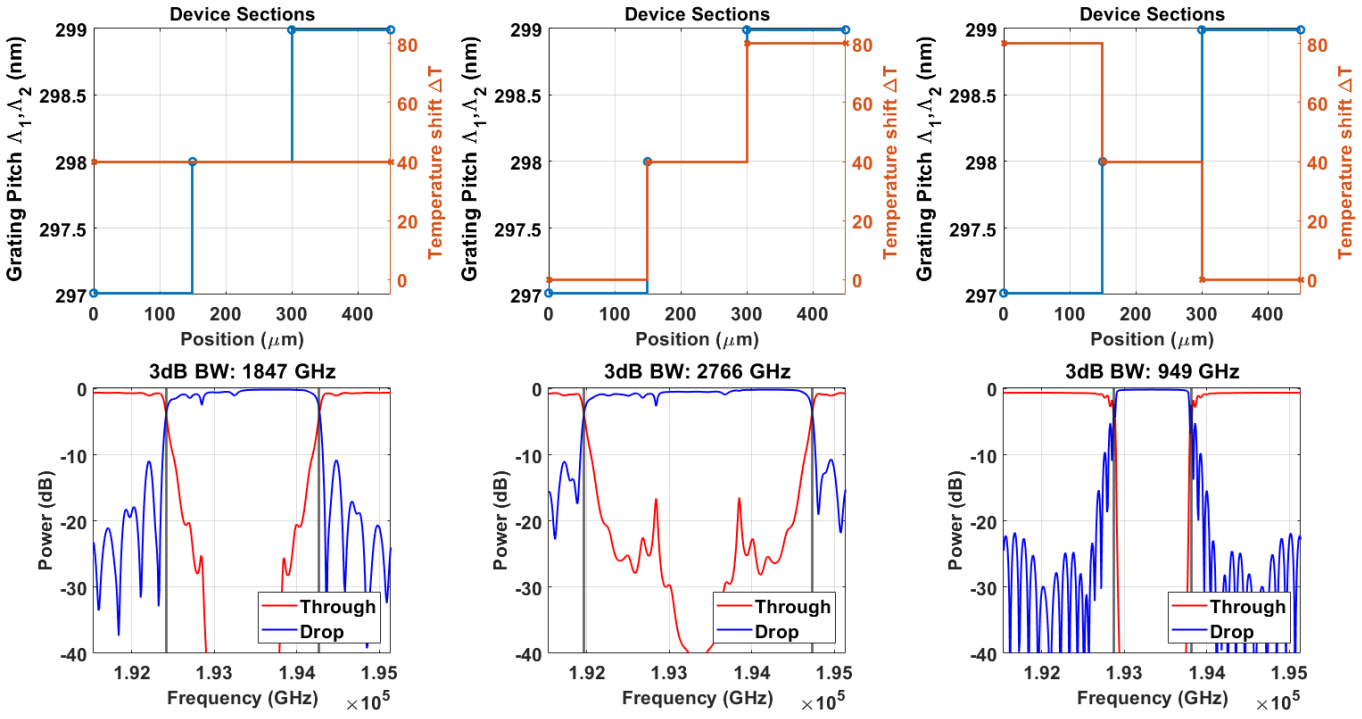

(a) (b) (c)

Fig. 8: Drop bandwidth for the first pitch-chirped device: **(a)** default state, **(b)** under positive thermal chirp, **(c)** under negative thermal chirp.

This signifies that the device can now operate on an extended bandwidth while still covering the smaller bandwidth of the original, single-pitch, structure, as the bandwidth tunability is largely increased, although without moving the lower bound. Of course, this technique cannot be extended indefinitely, as depending on the base bandwidth on the original device, multiple channel and response notches may appear when the phase-match regions stop overlapping: this has been tested by considering a device with higher pitch chirping range $\Lambda_1 = 296.5\,\text{nm}$, $\Lambda_2 = 298\,\text{nm}$, $\Lambda_3 = 299.5\,\text{nm}$. The response of this second pitch-chirped device is shown in Fig. 9, and as expected the maximum bandwidth increases even more, up to $\text{BW} = 3195\,\text{GHz}$ in the positive thermal gradient scenario. However, notches between the different spectral regions start to appear, which highlights the limiting case for the pitch-chirping technique. In Fig. 9b the notches are shown to be compensated by reducing the thermal step-size and considering five thermally controlled regions, instead of the previous three.

While a smoother thermal gradient can be used to compensate for the notches, and is still compatible with the initially considered ten-contact heater, the real limiting factor is visible when applying the negative gradient: the minimum bandwidth case (Fig. 9c) is now well above the reference case, as the negative gradient temperatures are not sufficient to overlap the phase match region back on the original wavelength. This highlights the upper bound in the bandwidth tunability range: the magnitude of the phase-match shift introduced by the pitch variation cannot be larger than the one achievable through thermal control; otherwise, the original bandwidth would not be included in the achievable responses. As a consequence, it is quite straightforward to see that pitch chirping can, at most, double the bandwidth tunability ΔBW for a given fixed thermal range: the chirped device will therefore have static bandwidth equal to the maximum achievable bandwidth of the original unchirped device. The minimum bandwidth $\Delta\lambda_{\text{min}}$, corresponding to a negative temperature gradient overlapping the multiple phase-match regions over the design central wavelength, will be equal to the reference bandwidth: a further decrease in the gradient after the minimum is reached will lead to a bandwidth increase due to the inversion of the left- and right-side phase-match conditions (similar to the symmetry shown in the unchirped device shown in Fig. 7).

Finally, the maximum bandwidth $\Delta\lambda_{\text{max}}$, obtained with the positive thermal gradient, will correspond to twice the increment of the original dynamic control, due to both the contributions of the pitch chirp and the additional thermal offsets. This phenomenon also justifies the division into three main pitches as well as three thermal regions in the analysis: adding additional points in either thermal or chirped profiles can only affect the smoothness or notches formation in the middle of the frequency response, while the limiting factors for the tunability range are still dictated by the highest and lowest achievable phase match conditions.

While these simulations assume ideal manufacturing, with exact pitch regions, the underlying principle still holds when considering fluctuations in the grating periodicity. While in the analysis the multiple static phase-match regions are obtained through chirping, the GACDC could be modelled with constant pitch, while varying the unperturbed core of the waveguide, leading to the control of the static phase-match condition through width modulation[35].

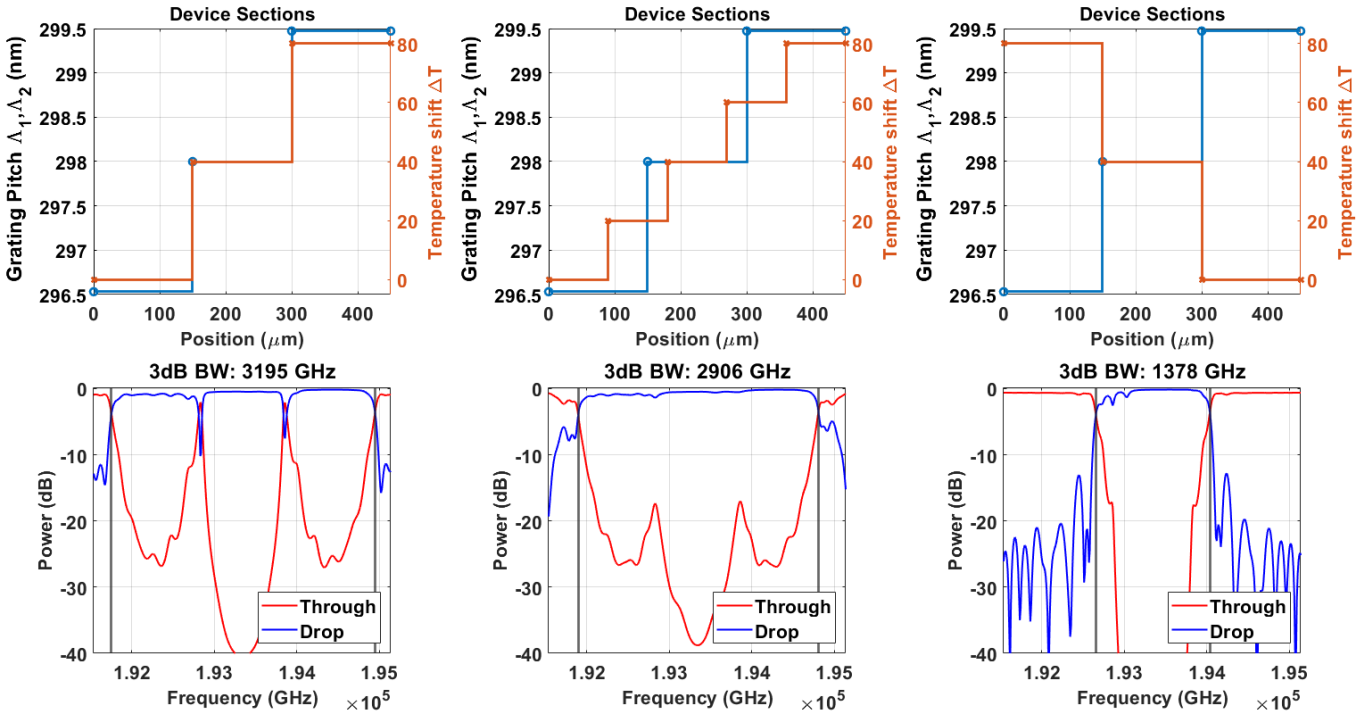

(a) (b) (c)

Fig. 9: Drop bandwidth for the second pitch-chirped device under positive thermal chirp with notches formation **(a)**, under reduced thermal chirp without no notches **(b)**, and under negative thermal bias **(c)**.

Moreover, any uncertainty is expected to affect the single-pitch device with a similar distribution as the chirped structures, so the increase in minimum bandwidth (and consequently lower coupling strength), due to spurious variation in pitch, would be visible in both cases, while not directly affecting the tunability range[28]. A qualitative example is depicted in Fig. 10, where the pitch is randomly varying following a gaussian distribution with the design pitch as mean ($\mu = [297,\ 298,\ 299]\ nm$) and $\sigma = 1\,\text{nm}$, rounded to the nearest integer nanometer. This introduces noticeable responsede gradation, with notches and asymmetric distortions. The minimum bandwidth is largely unaffected however, while the maximum bandwidth is more susceptible to the distortions. This can be compensated by optimizing the control scheme to account for the pitch variation, albeit slightly reducing the tunability range, which remains higher than the single-pitch case. Rigorous robustness simulations would require a large sample of experimental devices to model the uncertainty, which is outside of the current scope of the work, due to the focus on the theoretical limitations of pitch-based tunability enhancement.

C. General design principles

The results presented in the previous section are qualitatively clear and highlight the general principle of enhanced bandwidth tunability; however, they do not provide general guidelines for a GACDC with arbitrary bandwidth. In general, we can assume that devices that target telecom applications in the S, C, or L optical windows ($\lambda = 1.46\,\mu\text{m} - 1.625\,\mu\text{m}$) deployed on the Silicon Photonics SOI platform will have an average waveguide width between $W = 300\,\text{nm} - 650\,\text{nm}$, for which we can analyze the generic phase-match shift as a function of temperature or grating pitch change (Fig. 11a). The result shows that the phase-match tunability coefficients $\frac{d\lambda}{dT}$ and $\frac{d\lambda}{d\Lambda}$ do not vary significantly even for wide ranges of waveguide geometries, further enhancing the generality of the analysis: this result also proves how the temperature represents the limiting factor in tunability, as even a small variation of the pitch ($1 - 2\,\text{nm}$) can account for two orders of magnitude in temperature variation (in fact, the thermo-optical shift is depicted for $T = 100\,^\circ\text{C}$ in Fig. 11a).

While this investigation focuses on the thermo-optic (TO) effect as the main tunability mechanism, dynamic Silicon Photonic devices are also implemented leveraging the electro-optic (EO) effect [36]. While EO is faster than TO, albeit introducing higher losses, in this analysis the focus is mainly on tunability: considering that silicon exhibits a much larger TO coefficient with respect to the EO counterpart, the TO analysis can be generalized, considering that the alternative effect would impose an even lower index modulation.

Taking into account the constraint on thermal control imposed by the metallic heaters ($T_{\text{max}} \approx 100\,^\circ\text{C}$), we can evaluate the maximum range of the 3 dB bandwidth ΔBW. In the results discussed, the maximum tunability for an unchirped device corresponds to $\Delta BW \approx 606\,\text{GHz} \approx 5\,\text{nm}$ while the examples in the previous section show how the use of pitch chirping can extend the range up to $\Delta BW \approx 1149\,\text{GHz} \approx 11\,\text{nm}$.These values are not representative of the minimum or maximum bandwidth on their own, as shown in Fig. 9, which has a higher achievable maximum bandwidth, although also a higher minimum.

Minimum bandwidth

The static bandwidth of the GACDC is directly proportional to the coupling coefficient κ_{12}, which is shown in Fig. 11b for the proposed waveguide geometry: the simulation shows a

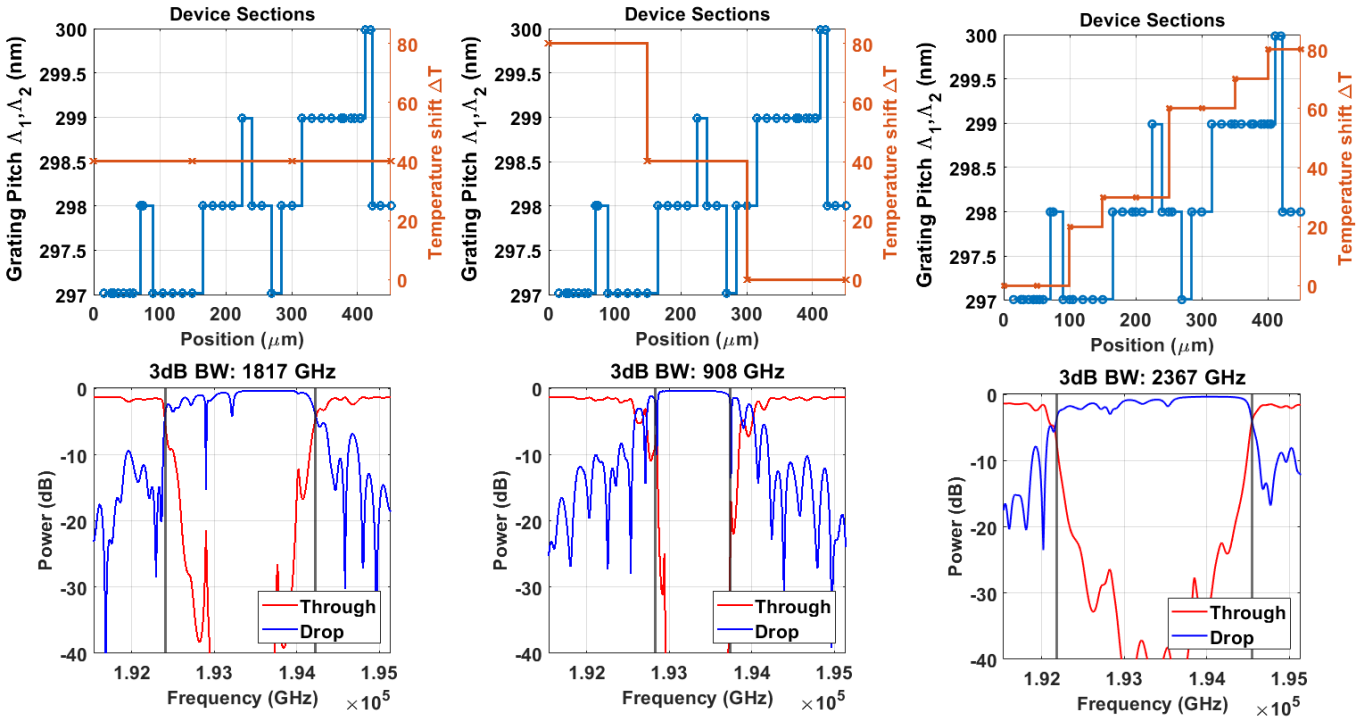

(a) (b) (c)

Fig. 10: Drop bandwidth considering pitch-fluctuations **(a)** default state, **(b)** under negative thermal chirp, **(c)** under positive thermal chirp.

linear relationship between the two, which is expected since the 3 dB drop bandwidth can be expressed through the CMT model as a function of the central wavelength of the channel, the group indices of the two waveguide modes n_{g1}, n_{g2}, and the coupling coefficient.

$$\Delta\lambda_{\min} \approx \frac{2\kappa_{12}\lambda_0^2}{\pi(n_{g1}+n_{g2})} \tag{1}$$

The minimum bandwidth can be set by engineering the waveguides' gap and geometry to obtain the desired coupling coefficient and group indices, although the device length must also be considered, as it represents the final limiting factor for the bandwidth tunability range. Fig. 12a depicts the drop response as a function of the coupling strength $\kappa_{12}L$, which is evaluated as the product of the coupling coefficient and the coupling length. The responses have been evaluated for a coupling coefficient $\kappa_{12} = 50\,\mathrm{cm}^{-1}$, although the result can be generalized for any coupling value κ_{12}. Fig. 12b shows the generalized trend, depicting the power coupled at the drop port for the 3 dB bandwidth of the phase-match channel (normalized against a ideal square filter with identical 3 dB bandwidth): normalization allows comparison of filter efficiency, which depends on both coupling coefficient and length, even though the bandwidth may vary, due to the dependency on k_{12} alone. It is clear that to achieve a smaller minimum bandwidth we require a low coupling factor κ_{12}, which in turn leads to a longer device to avoid losses and low roll-off. This is true not only for the central channel but for any phase-match region derived from either thermal control or pitch-chirping: when increasing the bandwidth through active tuning, each new phase-match section will have a smaller coupling length, leading to a rapid decline in transmitted power, especially for low-coupling gratings.

These results can now be used to gain some insight into the limitations of the tunability mechanism, considering both the effect of the pitch chirping and the limitations of the material indices and geometrical parameters.

Maximum bandwidth

The maximum achievable bandwidth $\Delta\lambda_{\max}$ is limited by the maximum temperature change achievable with the chosen heating technology ($T_{\max}$).

$$\Delta\lambda_{\max} = \Delta\lambda_{\min} + \left(\frac{d\lambda_0}{dT}T_{\max}\right) + \left(\frac{d\lambda_0}{d\Lambda}\Delta\Lambda_{\max}\right) \tag{2}$$

From the analysis on the pitch chirping we have demonstrated how in order to maintain the design $\Delta\lambda_{\min}$, the pitch chirp can only double the effect of the thermal control (i.e., $\frac{d\lambda_0}{dT}T_{\max} = \frac{d\lambda_0}{d\Lambda}\Delta\Lambda_{\max}$), therefore allowing simplification of Equation (2), removing the pitch dependency:

$$\Delta\lambda_{\max} = \Delta\lambda_{\min} + 2\frac{d\lambda_0}{dT}T_{\max} \tag{3}$$

Depending on the design, the pitch chirp must be selected to ensure that the above condition holds true.

Number of phase-match regions

The resulting tunability range $\Delta BW = \Delta\lambda_{\max} - \Delta\lambda_{\min}$ can be expressed as an integer multiple of the minimum bandwidth $N_{\min} = \left\lceil \frac{\Delta\lambda_{\max}}{\Delta\lambda_{\min}} \right\rceil$: $N_{\min}$ corresponds in this case to the minimum number of non-spectrally overlapping phase match regions, each with the same length L.

However, a larger number of sections can be used, e.g., to maximize the spectral uniformity of the drop channel response, as shown in the device analysis of the previous

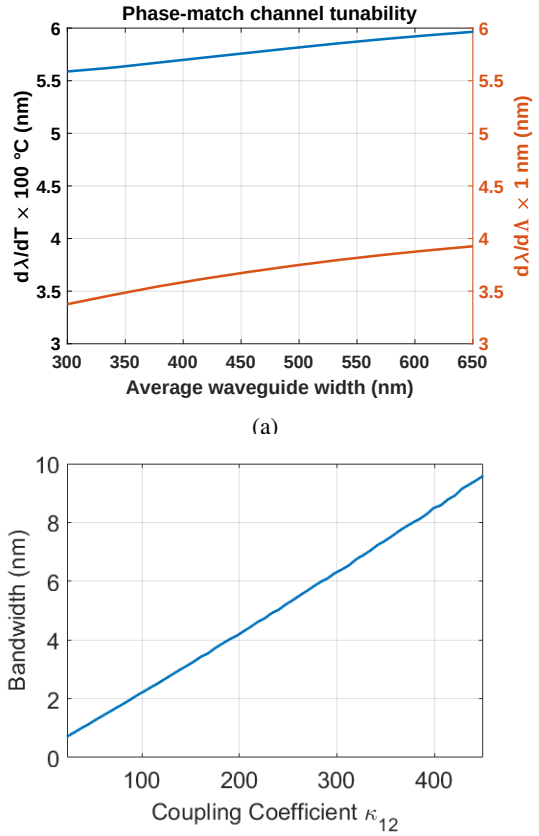

Fig. 11: **(a)** Phase-match wavelength tunability coefficients (left: thermal dependency, right: pitch dependancy) as a function of the waveguide widths. **(b)** Minimum bandwitdth of the CDC without thermal or pitch control, as a function of the contra-directional coupling coefficient.

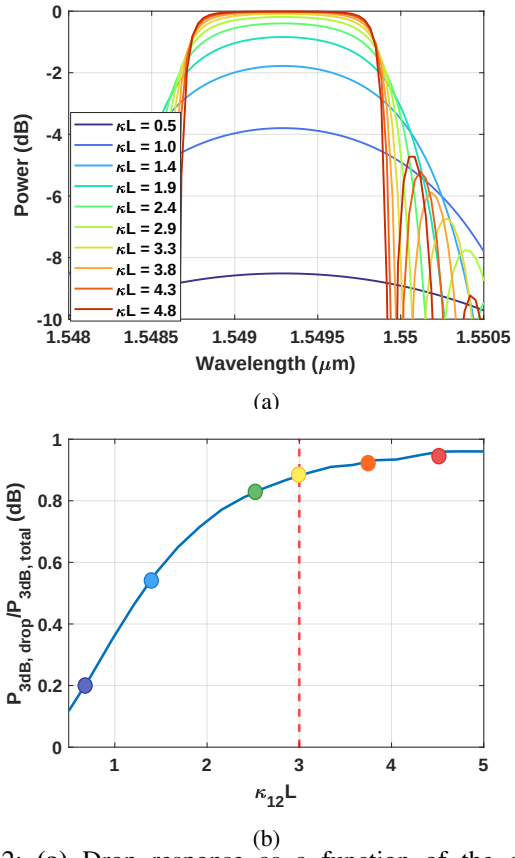

Fig. 12: **(a)** Drop response as a function of the coupling strength κL. **(b)** Normalized 3 dB coupled power as a function of the coupling strength (coupling factor times coupling length). The colored marker represents the curves depicted in (a)

section. However, the parameter N is useful for evaluating the necessary device length L_{tot} to ensure a steep roll-off and low drop channel loss: assuming, as stated, regions with uniform length $L_{\text{tot}} = NL$ and imposing a constraint on the coupled power in each region (e.g., $\kappa_{12}L > 3$, as discussed above), we obtain a constraint on the overall device length $L_{\text{tot}} > N\frac{3}{\kappa_{12}}$, which corresponds to the minimum overall length to ensure proper tunability in the desired range ΔBW.

D. Numerical design example

Looking back at the example of the previous section we see that for a starting $\Delta\lambda_{\text{min}} \approx 7.6\,\text{nm}$ (950 GHz) we require a coupling coefficient $\kappa_{12} \approx 300\,\text{cm}^{-1}$ to $350\,\text{cm}^{-1}$, which correspond to the geometrical design proposed.
Moreover, as previously highlighted, the thermal bottleneck $T_{\text{max}} \approx 80\,^{\circ}\text{C}$ corresponds to a $\Delta BW \approx 7.5\,\text{nm}$, leading to a maximum bandwidth $\Delta\lambda_{\text{max}} \approx 15\,\text{nm}$ (1900 GHz) for an unchirped device, and $\Delta\lambda_{\text{max}} \approx 22\,\text{nm}$ (2800 GHz) for a pitch-chirped solution.
This range lead to a minimum number of regions $N_{\text{min}} = 3$, which under the selected coupling strength constraint lead to a minimum length $L > 360\,\mu\text{m}$, compatible with the chosen length $L = 450\,\mu\text{m}$.

IV. Conclusion

The CMT model and COMSOL multiphysics solver have been used to showcase the use of index gradient control to manipulate the drop channel bandwidth of GACDCs. The traditional control through the thermo-optic effect has been evaluated, highlighting both its theoretical limitations, as well as the physical constraint imposed by the heater technology. Additional bandwidth-enhancing techniques such as pitch modulation have been considered in the device design and simulation: pitch-chirped design has been demonstrated as a tunability enhancement technique, allowing a twofold increase in dynamic bandwidth control.
The maximum range of this effect has been also investigated, showcasing the main limiting factors for the bandwidth control, either due to thermal limitation in the single-pitch device, or notches formation and spectral distortion in multi-pitch GACDC. The chirped design has been shown to double the effective tunability range while utilizing the same control mechanism with identical driving currents.
The general design rules have been derived for the enhanced structure, allowing quick analytical evaluation of both the achievable bandwidths and the constraint on the geometrical parameters, such as length, coupling, and minimum number of index-modulated regions.

V. Data availability

The datasets generated during the current study are available from the corresponding author upon reasonable request.

Acknowledgments

This work has been supported by Compagnia di San Paolo, PoC Instrument 2022-2024 (SCIPIO).

References

[1] S. Y. Siew, B. Li, F. Gao, H. Y. Zheng, W. Zhang, P. Guo, S. W. Xie, A. Song, B. Dong, L. W. Luo, C. Li, X. Luo, and G.-Q. Lo. Review of silicon photonics technology and platform development. *Journal of Lightwave Technology*, 39(13):4374–4389, 2021.

[2] Yikai Su, Yong Zhang, Ciyuan Qiu, Xuhan Guo, and Lu Sun. Silicon photonic platform for passive waveguide devices: Materials, fabrication, and applications. *Advanced Materials Technologies*, 5(8):1901153, 2020.

[3] Sudip Shekhar, Wim Bogaerts, Lukas Chrostowski, John E. Bowers, Michael Hochberg, Richard Soref, and Bhavin J. Shastri. Roadmapping the next generation of silicon photonics. *Nature Communications*, 15(1):751, Jan 2024.

[4] Tomoyuki Akiyama. Tutorial on silicon photonics applications. In *2023 Optical Fiber Communications Conference and Exhibition (OFC)*, pages 1–56, 2023.

[5] Keijiro Suzuki, Ryotaro Konoike, Hiroyuki Matsuura, Ryosuke Matsumoto, Takashi Inoue, Shu Namiki, Hitoshi Kawashima, and Kazuhiro Ikeda. Recent advances in large-scale optical switches based on silicon photonics. In *2022 Optical Fiber Communications Conference and Exhibition (OFC)*, pages 1–3, 2022.

[6] Masahiko Jinno, Takuya Ohara, Yoshiaki Sone, Akira Hirano, Osamu Ishida, and Masahito Tomizawa. Elastic and adaptive optical networks: possible adoption scenarios and future standardization aspects. *IEEE Communications Magazine*, 49(10):164–172, 2011.

[7] Nabarun Saha, Giuseppe Brunetti, Annarita Di Toma, Mario Nicola Armenise, and Caterina Ciminelli. Silicon Photonic Filters: A Pathway from Basics to Applications. *Advanced Photonics Research*, 5(10):2300343, October 2024.

[8] Vien Van. *Optical microring resonators: theory, techniques, and applications*. CRC Press, 2016.

[9] Lorenzo Tunesi, Andrea Carena, Vittorio Curri, and Paolo Bardella. Thermally-controlled transparency in multi-ring cascaded filters. In Graham T. Reed and Andrew P. Knights, editors, *Silicon Photonics XIX*, volume 12891, page 128910N. International Society for Optics and Photonics, SPIE, 2024.

[10] Folkert Horst, William M.J. Green, Solomon Assefa, Steven M. Shank, Yurii A. Vlasov, and Bert Jan Offrein. Cascaded mach-zehnder wavelength filters in silicon photonics for low loss and flat pass-band WDM (de-)multiplexing. *Opt. Express*, 21(10):11652–11658, 5 2013.

[11] Rafael Kraemer, Fumi Nakamura, Menno van den Hout, Sjoerd van der Heide, Chigo Okonkwo, Hiroyuki Tsuda, Antonio Napoli, and Nicola Calabretta. Multi-band photonic integrated wavelength selective switch. *Journal of Lightwave Technology*, 39(19):6023–6032, 2021.

[12] Manoranjan Minz and Ramesh Kumar Sonkar. Design of a hybrid mode and wavelength division (de)multiplexer based on contra-directional grating assisted couplers on the SOI platform. *Appl. Opt.*, 60(9):2640–2646, 3 2021.

[13] Yu He, Yong Zhang, Hongwei Wang, and Yikai Su. On-chip silicon mode blocking filter employing subwavelength-grating based contra-directional coupler. *Opt. Express*, 26(25):33005–33012, 12 2018.

[14] Lorenzo Tunesi, Ihtesham Khan, Muhammad Umar Masood, Enrico Ghillino, Vittorio Curri, Andrea Carena, and Paolo Bardella. Design and performance assessment of modular multi-band photonic-integrated wss. *Opt. Express*, 31(22):36486–36502, 10 2023.

[15] Wei Shi, Venkat Veerasubramanian, David V. Plant, Nicolas A. F. Jaeger, and Lukas Chrostowski. Silicon photonic Bragg-grating couplers for optical communications. In Atul K. Srivastava, editor, *Next-Generation Optical Networks for Data Centers and Short-Reach Links*, volume 9010, page 90100F. International Society for Optics and Photonics, SPIE, 2014.

[16] Nabarun Saha, Giuseppe Brunetti, Mario Nicola Armenise, and Caterina Ciminelli. Tunable narrow band add-drop filter design based on apodized long period waveguide grating assisted co-directional coupler. *Opt. Express*, 30(16):28632–28646, Aug 2022.

[17] Debin Mu, Huiye Qiu, Jianfei Jiang, Xiaofei Wang, Zhilei Fu, Yuehai Wang, Xiaoqing Jiang, Hui Yu, and Jianyi Yang. A four-channel dwdm tunable add/drop demultiplexer based on silicon waveguide bragg gratings. *IEEE Photonics Journal*, 11(1):1–8, 2019.

[18] Huiye Qiu, Jianfei Jiang, Ping Yu, Debin Mu, Jianyi Yang, Xiaoqing Jiang, Hui Yu, Rui Cheng, and Lukas Chrostowski. Narrow-band add-drop filter based on phase-modulated grating-assisted contra-directional couplers. *J. Lightwave Technol.*, 36(17):3760–3764, 9 2018.

[19] Wei Shi, Xu Wang, Charlie Lin, Han Yun, Yang Liu, Tom Baehr-Jones, Michael Hochberg, Nicolas A. F. Jaeger, and Lukas Chrostowski. Silicon photonic grating-assisted, contra-directional couplers. *Opt. Express*, 21(3):3633–3650, 2 2013.

[20] M. T. Boroojerdi, M. Ménard, and A. G. Kirk. Two-period contra-directional grating assisted coupler. *Opt. Express*, 24(20):22865–22874, 10 2016.

[21] W. Shi, X. Wang, W. Zhang, L. Chrostowski, and N. A. F. Jaeger. Contradirectional couplers in silicon-on-insulator rib waveguides. *Opt. Lett.*, 36(20):3999–4001, 10 2011.

[22] J.-P. Weber. Spectral characteristics of coupled-waveguide bragg-reflection tunable optical filter. *IEE Proceedings J (Optoelectronics)*, 140:275–284(9), 10 1993.

[23] https://www.synopsys.com/photonic-solutions.html.

[24] Mohammad Amin Mahdian, Lorenzo Tunesi, Paolo Bardella, and Mahdi Nikdast. Bandwidth-adaptive single- and double-channel silicon photonic contra-directional couplers. In *2023 IEEE Photonics Conference (IPC)*, pages 1–2, 2023.

[25] Debin Mu, Huiye Qiu, Jianfei Jiang, Xiaofei Wang, Zhilei Fu, Yuehai Wang, Xiaoqing Jiang, Hui Yu, and Jianyi Yang. A four-channel DWDM tunable add/drop demultiplexer based on silicon waveguide Bragg gratings. *IEEE Photonics Journal*, 11(1):2897359, 2 2019.

[26] Y. T. Aladadi, A. F. Abas, and M. T. Alresheedi. Optimum apodization profile for chirped fiber bragg gratings based chromatic dispersion compensator. *Journal of the European Optical Society-Rapid Publications*, 12(1):6, 6 2016.

[27] Wei Shi, Mark Greenberg, Xu Wang, Yun Wang, Charlie Lin, Nicolas A. F. Jaeger, and Lukas Chrostowski. Single-band add-drop filters using anti-reflection, contra-directional couplers. In *The 9th International Conference on Group IV Photonics (GFP)*, pages 21–23, 2012.

[28] M. Hammood, Ajay Mistry, Han Yun, Minglei Ma, Stephen Lin, Lukas Chrostowski, and Nicolas A. F. Jaeger. Broadband, silicon photonic, optical add–drop filters with 3 db bandwidths up to 11 thz. *Opt. Lett.*, 46(11):2738–2741, 6 2021.

[29] Lorenzo Tunesi, Mohammad Amin Mahdian, Andrea Carena, Vittorio Curri, Mahdi Nikdast, and Paolo Bardella. Segmented design and control in contra-directional couplers for large bandwidth tunability. In Shibin Jiang and Michel J. F. Digonnet, editors, *Optical Components and Materials XXI*, volume 12882, page 128820B. International Society for Optics and Photonics, SPIE, 2024.

[30] Dan-Xia Xu, André Delâge, Pierre Verly, Siegfried Janz, Shurui Wang, Martin Vachon, PengHui Ma, Jean Lapointe, Daniele Melati, Pavel Cheben, and Jens H. Schmid. Empirical model for the temperature dependence of silicon refractive index from o to c band based on waveguide measurements. *Opt. Express*, 27(19):27229–27241, Sep 2019.

[31] Applied Nanotools. NanoSOI MPW design rule. https://www.appliednt.com/nanosoi/sys/resources/rules/.

[32] Jonathan Cauchon, Jonathan St-Yves, and Wei Shi. Thermally chirped contra-directional couplers for residueless, bandwidth-tunable bragg filters with fabrication error compensation. *Opt. Lett.*, 46(3):532–535, 2 2021.

[33] Pedro Andrei Krochin Yepez, Ulrike Scholz, Jan Niklas Caspers, and Andre Zimmermann. Novel measures for thermal management of silicon photonic optical phased arrays. *IEEE Photonics Journal*, 11(4):1–15, 2019.

[34] Lorenzo Tunesi, Mohammad Amin Mahdian, Vittorio Curri, Andrea Carena, Mahdi Nikdast, and Paolo Bardella. Thermal control scheme in contra-directional couplers for centered tunable bandwidths. In *2023 International Conference on Numerical Simulation of Optoelectronic Devices (NUSOD)*, pages 115–116, 2023.

[35] C. J. Glassbrenner and Glen A. Slack. Thermal conductivity of silicon and germanium from 3°K to the melting point. *Phys. Rev.*, 134:A1058–A1069, 5 1964.

[36] Qianfan Xu, Bradley Schmidt, Sameer Pradhan, and Michal Lipson. Micrometre-scale silicon electro-optic modulator. *Nature*, 435(7040):325–327, May 2005.